Oxide dependent wear mechanisms of titanium against a steel counterface: Influence of SMAT nanostructured surface

Pierre Maurel, Laurent Weiss, Philippe Bocher, Eric Fleury, Thierry Grosdidier

Oxide dependent wear mechanisms of titanium against a steel counterface: Influence of SMAT nanostructured surface

Pierre Maurel[a,b,c,**], Laurent Weiss[a], Philippe Bocher[b], Eric Fleury[a,c], Thierry Grosdidier[a,c,*]

[a] Université de Lorraine, Laboratoire LEM 3, UMR CNRS 7239, 7 Rue Félix Savart, 57073, Metz, France
[b] Laboratoire d'Optimisation des Procédés de Fabrication Avancés (LOPFA), École de Technologie Supérieure, 1100 rue Notre-Dame Ouest, Montréal, Canada
[c] LABoratoire d'EXcellence "Design of Alloy Metals for low-mAss Structures" (LABEX-DAMAS), 7 rue Félix Savart, 57073, Metz, France

ARTICLE INFO

Keywords:
Oxidative degradation
Surface mechanical attrition treatment (SMAT)
Titanium
Wear transitions

ABSTRACT

The analysis of the tribological behavior of a steel ball on pure titanium has been carried out under alternative motion on both, a coarse grained Ti surface and its nanostructured derivative obtained by surface mechanical attrition treatment (SMAT). Along the duration of the tribology test, variations in friction behavior were interpreted as a three stages sequence of different wear mechanisms that were controlled by the successive formation of Ti-rich and Fe-rich oxides. Surface nanostructures appeared to change the oxide formation kinetics and delay the formation of a protective Fe-rich third body oxide layer on Ti. The results indicate that apparently contradicting literature results can be explained by taking into account the contamination induced during the SMAT process.

1. Introduction

Nanostructured microstructures manufactured by severe plastic deformation (SPD) processes often develop enhanced mechanical properties such as strength, hardness and fatigue resistance at the cost of a reduced ductility [1–3]. Among the existing SPD processes, the most commonly applied methods to produce nanostructured materials in bulk forms are equal channel angular pressing (ECAP) [4], high pressure torsion (HPT) [5], and accumulative roll bonding [6]. These methods can be rather difficult to implement since they require high loads to deform bulk samples and are thus restricted to rather fairly small bulk size. An interesting approach is to concentrate the deformation on the surface of materials with the essential goal of strengthening the critical locations where most degradations generally initiate (cracks, scratches, corrosion, fatigue, …). Thus, several techniques have been studied, and potentially applied for industrial applications such as shot-peening [7], laser shock peening [8] or burnishing [9] as well as Surface Mechanical Attrition Technique (SMAT) [10], also called Ultrasonic Shot-Peening (USSP) [11]. This last technique, consists by mean of a vibrating sole in propelling balls that hit the sample surface with different incident angles. With the goal of improving the mechanical properties of the surface, the later treatments have been applied on Cu [12], Mg [13,14], Al alloys [15],steels [16–20] and Ti [21,22] to introduce a deformation gradient at the top surface. The deformation behavior of commercially pure titanium after SMAT has been described by Zhu et al. [21]. Tribological properties of nanostructured alloys obtained by severe plastic deformation have been tested on steels [17], Ti [22,23], Al and Al_2O_3 composites [24] as well as Mg [13,14]. However, no general trends could be worked out to explain the wear resistance reported for alloys treated by SMAT [13,14,17]. Indeed, some results were apparently contradicting for both steels and Mg alloys. For example, though the SMAT and friction conditions were highly similar, some authors noted a reduction in wear loss for the AZ31 Mg alloy [13] whereas for the Mg-6Gd-3Y-0.5Zr authors observed an increase in wear loss [14]. On steels, Sun [17] has explained some incoherences by taking into account the high severity of unlubricated contact and the hardening already sustained by the samples treated by SMAT. This author also noted a significant improvement in the wear resistance for lubricated contact [17], while the plastic deformation was more predominant. Thus, the higher hardness of SMAT treated samples tended to prevent the local plastic deformation of the surface which, in turn, increased significantly the wear resistance [17]. Ti has been also investigated. Alikhani Chamgordani et al. [22] observed a significant reduction in wear loss for commercially pure titanium samples treated by low frequency SMAT for several hours. The tests were conducted at a relatively high speed of 230 mm/s with a 3 N load and a 275 m total sliding distance. Wen et al. [25] also noted a reduction in wear loss for tests conducted at 50 mm/s with loads of 1, 2

* Corresponding authors. Université de Lorraine, Laboratoire LEM 3, UMR CNRS 7239, 7 Rue Félix Savart, 57073, Metz, France.
** Corresponding authors. Université de Lorraine, Laboratoire LEM 3, UMR CNRS 7239, 7 Rue Félix Savart, 57073, Metz, France.
E-mail addresses: pierre.maurel@univ-lorraine.fr (P. Maurel), thierry.grosdidier@univ-lorraine.fr (T. Grosdidier).

and 5 N on commercially pure titanium treated by SMAT on a limited 30 m total sliding distance.

The aim of this work is to gain new insights in the understanding of the tribological properties of Ti and investigate in details the potential of SMATed commercially pure titanium at room temperature under unlubricated condition and at relatively low sliding speed. Thus, compared to previous works [22,25], this paper proposes a deep understanding of the wear mechanisms and their origin for the titanium-steel contact by the determination of the nature of the oxides formed, where and when they appeared and how they affected the friction. Potential industrial applications of this titanium-steel contact are in the manufacturing of steels parts when titanium friction pads are used to guide the work piece during processing as well as for aeronautical applications where titanium is widely used.

2. Methodology

2.1. Materials and treatment

A commercially pure titanium T50A - generally used in aerospace applications - with an initial average grain size of ASTM 5.5 to 6 (from 40 to 48 µm) was bought from the TIMET company (France). The chemical composition of this alloy was [wt%]: Fe 0.02, C 0.005, O 0.16, N 0.002 and Ti (balance). 10 mm thick samples were cut from a 30 mm diameter bar and then successively polished with SiC papers from 320 to 2000 grit before the SMAT treatments.

This T50A has been investigated under two different conditions:

i. The initial coarse grained samples after the 2000 grit polishing procedure
ii. The same polishing followed by a Surface Mechanical Attrition Treatment (SMAT).

Samples were ultrasonically shot peened to carry out the SMAT using a vibrating Stressonic device commercialized by SONATS [26], within a treatment chamber developed by Novelli et al. [19] and a titanium sonotrode. The samples were treated for 10 min at a distance of 20 mm from the vibrating part, which was moved at a frequency of 20 kHz for an amplitude of 60 µm. The same quantity of 2 mm diameter AISI 52100 steel shots, covering roughly 20% of the vibrating area, was used for each treatment.

2.2. Tribology tests

Tribology tests were carried out with an Anton-Paar TRB^3 pin-on-disk tribometer. The tribometer was used in its linear configuration with a 6 mm diameter AISI 52100 steel ball counterface having a hardness of 840 HV. The sample surfaces were ultrasonically cleaned with acetone and ethanol before the tribology tests to remove any oil or particles that might affect friction tests. A 2 N load was applied over a linear length of 10 mm for a frequency of 0.5 Hz. The sliding speed follows a sinusoidal variation with a maximum of 16 mm/s achieved in the middle of the groove length. The acquisition frequency was 50 Hz. A 6 mm length located at the center of the 10 mm long groove was determined as the zone of interest in which the sliding speed was always over 10 mm/s. The values of the coefficient of friction reported in the present work are the average values acquired over this 6 mm long region of interest. Sliding tests were carried out at room temperature under ambient air with a relative humidity varying from 30% to 50%. For each condition, five samples were prepared and tested (10 000 cycles for each condition corresponding to a 200 m total sliding distance). All these tests were carried out with the same procedure using a single set of parameters. In order to understand how the tribological and wear behaviors varied during the friction tests a second set of tests were stopped after 2000 cycles (40 m) for each sample conditions and a third set was stopped at 1500 cycles (30 m) for the SMATed surface only. The debris on the tested surfaces were collected after the tribology test, fixed on carbon pellets, and characterized in terms of size, chemical composition and morphology.

2.3. Microstructure and wear characterization

Microhardness surface measurements were done on the top surface with a 500 gf load and 5 measurements were carried out. The surface roughness was measured with an average of 6 measurements using a stylus surface profilometer. The topologies of the grooves and the ball counterfaces were investigated by confocal microscopy using an Olympus LEXT4100 apparatus and by focus-variation microscopy using an Alicona Infinite Focus apparatus.

Cross-section observations were made by scanning electron microscopy (SEM)after mirror polishing with diamond paste and colloidal silica suspension. The cross-section microstructure analyses as well as observations of the grooves, wear debris and the aspect of the steel ball surface degradations after the tribology tests were done by SEM using a ZEISS Supra 40 apparatus. Chemical composition mappings were obtained in this microscope by electron diffraction spectroscopy (EDS) using a Bruker XFlash 6|60 attachment.

Raman spectroscopy was carried out with a Raman HR Evolution apparatus from Horiba, using a 532 nm Oxxius laser. Measurements were acquired with a power of 4 mW, a magnification of 500× and an acquisition time of 10 s. The spectral range of interest is from 150 cm^{-1} to 800 cm^{-1}. Raman mappings were acquired with a step of 20 µm in the perpendicular direction of the sliding direction and a step of 50 µm in the same direction as the sliding. Grids of 300 lines/mm and of 1800 lines/mm were used. Raman peaks for titanium and iron oxides are available in the literature: TiO_2-Anatase presents peaks at **144**, 198, 320, **397**, 516, **639**, 695 and 795 cm^{-1}, TiO_2-Rutile at 143, 235, 273, 320, 357, **449**, **610**, 832 cm^{-1} [27], Fe_2O_3-Maghemite at 265, 300, 345, 395, 515, **645**, **670** and **715** cm^{-1}, and Fe_2O_3-Hematite at **225**, 245, **295**, **415**, 500 and 615 cm^{-1} [28]. The peaks written in bold characters are the high intensity modes: they are the most intense peaks expected in the spectra.

3. Results

3.1. SMAT modifications

A SEM analysis of a SMATed sample on cross-section is given in Fig. 1. The upper-surface of the cross-section in Fig. 1a, taken at low magnification, shows a gradient microstructure: coarse grains can be seen at the bottom, toward the material core, and smaller ones at the surface within a depth of about 100 µm. The top surface curvature with a shallow valley is due to a ball impact occurring during the SMAT process. Consistently with several previous investigations of SMATed surfaces, and in particular with studies carried out on commercially pure Ti [21,22,25], a layer containing sub-micrometer or even nano-size grains is detected at the top surface within a few tens of µm. In our case, these sub-micrometer grains - as illustrated in the higher magnification image Fig. 1b - were revealed over a thickness of about 30 µm. This 30 µm thick layer of sub-micrometers grains corresponds to the region that was mechanically loaded during the tribology tests. This is consistent with the pioneer work of Zhu et al. on commercially pure titanium [21] Only at about 100 µm below the surface are visible the initial grains that contain suggested marks of plastic deformation.

SMAT increased the top surface hardness by about 50%, as seen by the data given in Table 1. Table 1 also gives the surface roughness in the form of Ra (arithmetical mean deviation of the profile) and Rz (average of the heights between the five highest peaks and lowest valleys). SMAT resulted in a 20 times increase of both Ra and Rz values when compared to the polished initial surfaces. It is interesting to stress here that the Rz value is comparable to the typical depth of wear tracks measured after the tribology tests in several other studies [22,25]. As will be discussed

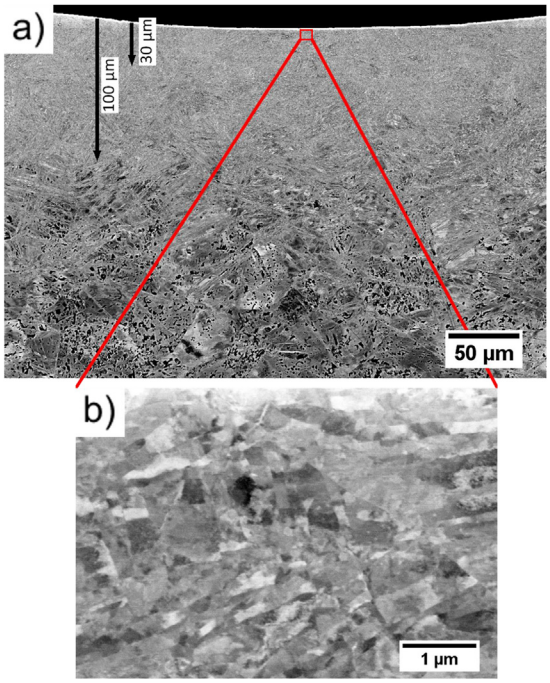

Fig. 1. SEM cross-section microstructure of the SMATed sample (a) and focus on the top surface microstructure (b)

Table 1
Ball worn area measurement and corresponding stages when the tests were finished for Initial and SMATed samples.

Sample	Worn area (mm^2) and stopping stage	
	2000 cycles	10 000 cycles
Initial	0.892 –beginning ofStage III	1.109 – Stage III
SMAT	0.315 – beginning ofStage II	0.728 – Stage III

in section 4.2., this has a potential effect on the discrepancies of the wear volume recorded for SMATed surfaces. Finally, Table 1 gives the volume losses measured after 10 000 cycles of sliding tests (200 m of total sliding distance). These results will be further detailed in part 3.3.

3.2. Friction behavior

Fig. 2 shows typical evolutions of the coefficient of friction as a function of the number of cycles recorded on samples of initial condition (Fig. 2a and b) as well as after SMAT (Fig. 2c and d). All the tests shared some similar trends for the general evolution of the coefficient of friction. Within the first tens of cycles, the coefficient of friction increases sharply during an initial break-in (BI) period, this period is followed by a steady-state regime with a value of the coefficient of friction reaching 0.5. This stage (called hereafter “stage I″) is followed by the occurrence of important irregularities perturbing the steady-state, this is stage II. The occurrence of irregularities continues until another steady-state regime (stage III) is reached. The coefficient of friction increases slightly towards values of about 0.6–0.7. For a given type of samples some discrepancies in the number of cycles at which these successive changes occurred were recorded. However, analyses of five tested samples for each condition (Initially polished or SMATed) have shown clear trends in the occurrence of the transition T1 between stage I and stage II and the transition T2 between stage II and stage III, as well as for the length of stage II. This is depicted in Fig. 3 in the form of histograms having a bin width equal to 1000 cycles. As illustrated in Fig. 3a, the transitionT1 always occurred before 1000 cycles for the initial samples. Comparatively the SMATed samples revealed a broader range of variability in the onset of the instabilities. For the initial sample, the length of stage II was also always shorter than the ones recorded for the SMATed samples (Fig. 3c). In consequence, the number of cycles to reach T2 was also shorter for the initial polished sample. It is also interesting to notice that the end of the unsteady regime (stage II) could not be reached for one of the sliding experiments performed onto the SMATed surface.

3.3. Wear profiles and wear loss

The cross section profiles of five worn tracks were recorded with the same set of sliding parameters (load, frequency, …) and the same number of cycles (10 000 cycles) for each of the two types of surfaces. Each wear profile displayed in Fig 4 is an average of the heights along the longitudinal axis of the 6 mm central zone of interest obtained from the 3D topography analysis. The profiles show grooves around 1.1 or 1.2 mm wide with a varying depth, the maximum depth is toward the center of the groove on the transversal axis. In Fig. 4a, except for one sample, the initial samples systematically revealed similar wear profiles with a maximum depth variation generally lower than 10 µm. The initial samples also revealed bulges on the sides of the grooves (red arrowed in Fig. 4a). Comparatively, the SMATed samples were characterized by a larger variation of the maximum groove depth; up to 26 µm. It is also interesting to note the overall absence of bulges on the sides of the grooves made on the SMATed surface.

The trends concerning the average depth of the grooves are confirmed by the mean volume losses displayed in Table 1. It is remarkable to note that the initial samples have an amount of material removal twice lower in comparison with the SMATed ones.

3.4. Wear observations of the titanium surfaces

SEM observations of the wear grooves of SMATed surfaces for different friction durations, (i.e. 1 500, 2000 and 10 000 cycles) corresponding to interruptions during the stages I, II and III, respectively are shown in Fig. 5. The grooves are around 750 µm wide after both 1500 cycles and 2000 cycles, the width increases to 1 mm for 10 000 cycles. Corresponding EDS maps of Fe are presented in transparency of red in Fig. 5a, b and 5d for the area of interest. Peaks and valleys (arrowed in red in Fig. 5a, b and 5c) due to the SMAT are visible on both sides of the different grooves, evidencing the increased roughness. In Fig. 5a, during stage I, the groove has clear wear marks along the sliding direction mostly originating from surface ploughing and micro-cutting. These marks suggest a dominating abrasive wear mechanism. Few asperities were also observed in the groove, suggesting the occurrence of some adhesion wear. However, the contribution of adhesion to the total wear was rather low. At stage II, SEM observations such as the one in Fig. 5b showed abrasive wear marks along the sliding direction similar to those made during stage I (Fig. 5a). However, more irregularities and asperities, as those pointed by white arrows in Fig. 5b, were revealed; indicating a larger contribution of the adhesive wear during stage II. While nearly no sign of Fe was detected by EDS mapping in the observed zone in Fig. 5a, the EDS map in Fig. 5b reveals the presence of a thin discontinuous band of iron at the very center of the groove along the sliding direction. It is interesting to notice that most of the asperities are located in the Fe-rich areas, indicating that stage II is characterized by metal transfers from the steel ball onto the Ti surface. At stage III, Fig. 5c illustrates that the observed wear tracks presented a high density of asperities covering most of the groove, indicated by white arrows. The comparison between the image and EDS map in Fig. 5c and d shows that most asperities are observed in connection with Fe-rich areas. Thus, during stage III, the tribo-oxidative wear becomes predominant in the groove and a large Fe-rich transfer layer was formed, owing to the wear of the steel ball. Observations of the wear tracks in the few Fe-free regions showed, once again, abrasive wear marks along the sliding direction.

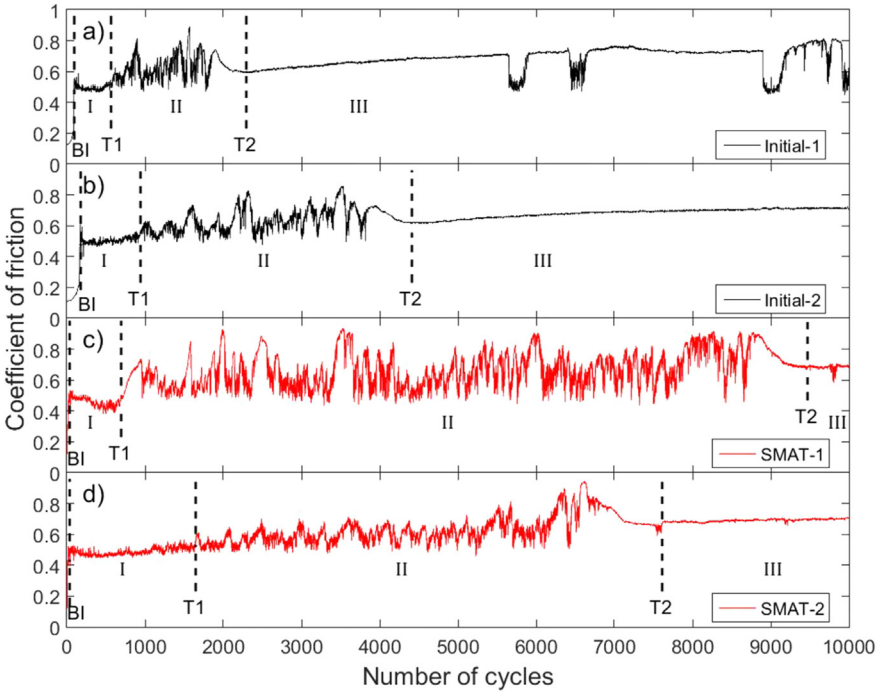

Fig. 2. Evolution of the sliding behavior for initially polished (a and b) and SMATed (c and d) samples, 3 successive stages indicated as I, II and III separated by T1 and T2. Break-in duration also indicated as BI

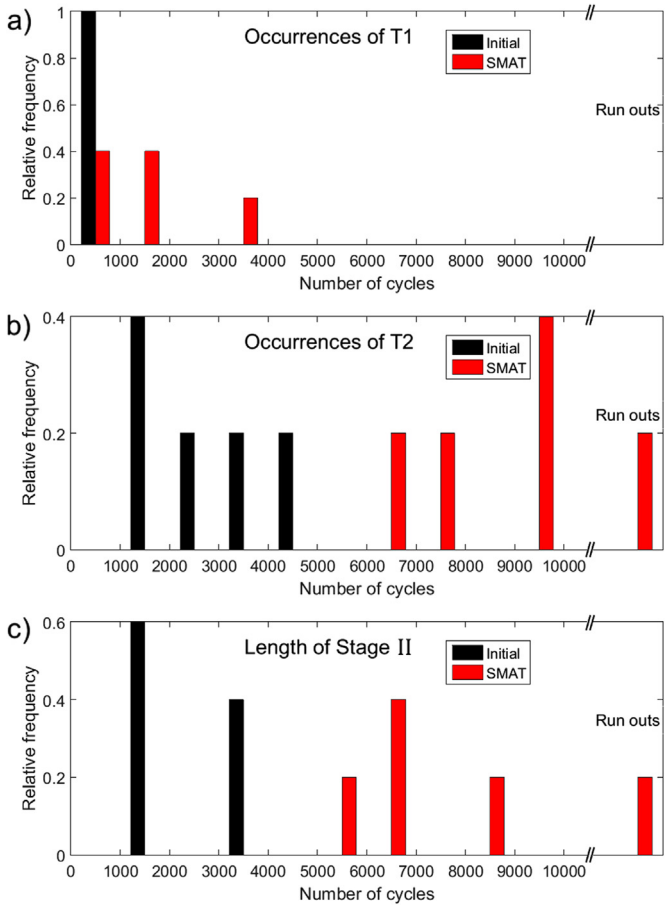

Fig. 3. Histograms of appearances of T1 (a) and T2 (b) characteristic times and histogram of stage II length (c) with 1000 cycles bin width for five friction tests of 10 000 cycles on each surface conditions

Fig. 6 gives an analysis of the wear groove during stage III (i.e. after 10000 cycles) for the initially polished sample. The central part of the wear groove displays an irregular topology with asperities, as seen in Fig. 6a. The associated EDS map represented in transparency of red in Fig. 6a confirms that the Fe-rich domains formed this irregular topology. Fig. 6b shows a higher magnification image in which the zone designed by the white ellipse corresponds to a large Fe-rich particle. This particle seems to be constituted of several smaller particles that coalesced by friction and is surrounded by much smaller Fe-rich particles. In his theory of the third-body, Godet highlighted several different debris behaviors [29]. Among those mentioned, one is very close to one observed here: powders coalescing under even low pressure fields.

3.5. *Wear observations of the steel counterface*

In addition to the worn Ti surface analyses, the sliding steel ball counterfaces were also observed by SEM in order to characterize efficiently the tribology system as a whole.

SEM observations on the steel counterfaces after 2000 cycles of sliding against the SMATed surface (Fig. 7a) and against the initial surface (Fig. 7b) show that the steel balls were damaged and the worn areas are clearly visible in these images. In these cases, the friction tests were stopped during stage II (Fig. 7a) and stage III (Fig. 7b), respectively. The corresponding Ti EDS maps, in transparency of green in Fig. 7a and b, show titanium particles at the periphery of the worn areas. Titanium was also present within the worn area of the steel counterface stopped during stage II; confirming thereby the deposition and adhesion of titanium wear debris on the ball during stage II. Heinrichs et al. [30] have highlighted the high adhesion of titanium and its ability to form a transfer layer on several counterface materials; and steel was among them. This adhesion tendency explains the titanium deposition observed on the steel ball. In Fig. 7b, it is interesting to notice also the absence of titanium in this central area of the counterface during stage III. As will be discussed later, this is a complementary information that attests a change in wear mechanism between stage II and stage III.

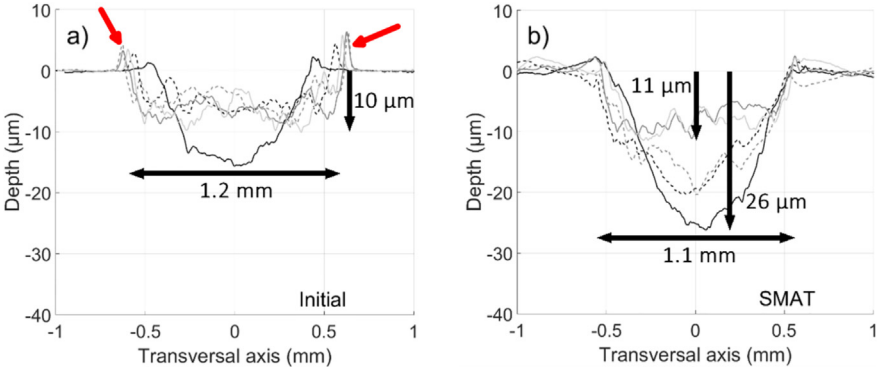

Fig. 4. Mean wear profiles of five friction tests against initially polished (a) and SMATed (b) surfaces over the central 6 mm of the groove for a single set of parameters and 10 000 cycles

The worn areas of Fig. 7a and b were measured and their surfaces are given in Table 2. For the same number of cycles (2 000) the ball sliding against the initially polished surface shows a worn area three times larger than the one measured on the ball that has slided against the SMATed surface. Additionally, the worn areas obtained after 10 000 cycles was also measured for both the initial surface and the SMATed surface (Table 2), the friction was stopped during stage III. Again, for the 10 000 cycles counterfaces rubbing against the initially polished surface produced a 50% wider damaged area than when the rubbing was done against the SMATed surfaces. Interestingly, while the worn areas of the steel ball sliding against the initial surface was only increased by 20% between 2000 and 10 000 cycles, the SMATed surfaces generated a worn area on the steel ball more than twice as large between 2000 (stage II) and 10 000 cycles (stage III). This suggests that, despite the instabilities that are the typical feature of stage II, the wear rate of the steel ball counterface is significantly higher in stage II than during stage III.

3.6. Oxide characterization

Raman spectroscopy was carried out in order to characterize the nature of the oxides issued from the friction tests and to understand the evolution of the coefficient of friction. Fig. 8a and c shows optical microscopy images of grooves obtained on SMATed surfaces and resulting from 2000 cycles (stage II) and 10 000 cycles (stage III) of friction, respectively. Fig. 8b and d represent their reconstructed maps obtained by Raman spectroscopy, while their corresponding Raman spectra are given in Fig. 8e and f, respectively. While the spectra allowed to determine locally the nature of oxides, the Raman maps allowed to represent their locations within the groove. In Raman spectroscopy, the ratio between the peak intensity and the baseline determines an arbitrary unit value for the mapping. In both optical images of the groove (Fig. 8a and c) wear marks along the sliding direction as well as irregularities of SMATed surfaces are clearly visible, similar to the observations in Fig. 5. Fig. 8a shows the same groove as the one in Fig. 5b, thus the dark areas (Zone 2) at the groove center are the Fe-rich domain of the transfer layer. In Fig. 8c, the large dark spots (Zone 4) are also the Fe-rich transfer layer. Fig. 8b and d were constructed from the intensity of the shaded areas of the Raman spectra in Figs. 8e and f.

The zone 1 outside of the groove in Fig. 8a corresponds to the treated surface and the corresponding spectra in Fig. 8e show only one peak at around 500 cm^{-1}. No iron was detected in this area outside of

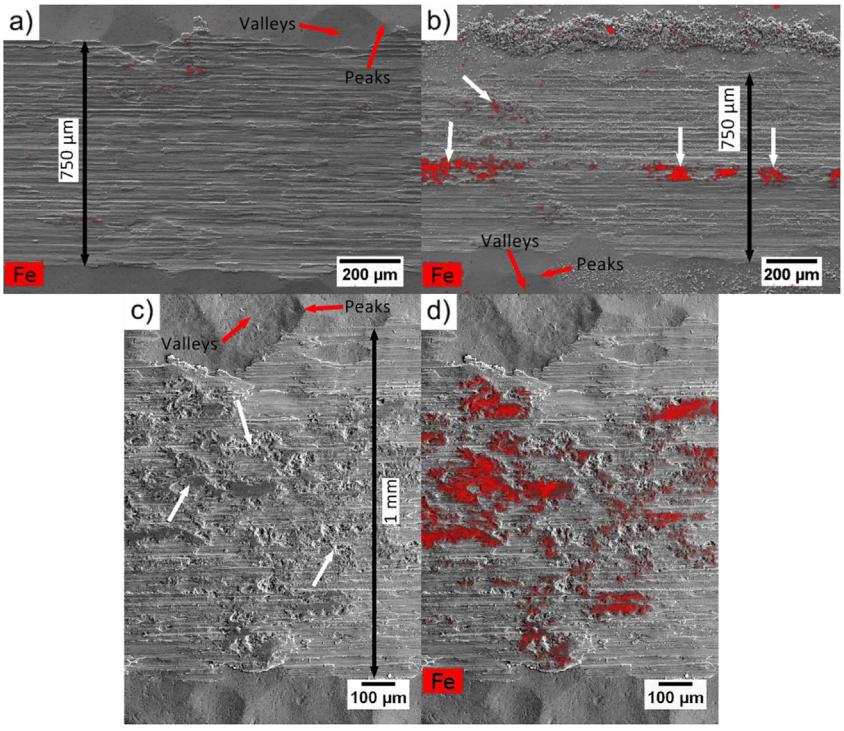

Fig. 5. SEM images of the wear groove after 1 500 cycles (a) and after 2 000 cycles (b) on SMATed sample stopped during Stage I with Fe (red) EDS map in transparency above. SEM image of the wear groove after 10 000 cycles on SMATed sample stopped during Stage III (c) and the same image with Fe (red) EDS map in transparency (d). The red arrows indicate the peaks and valleys of the surface outside of the groove. White arrows indicate asperities

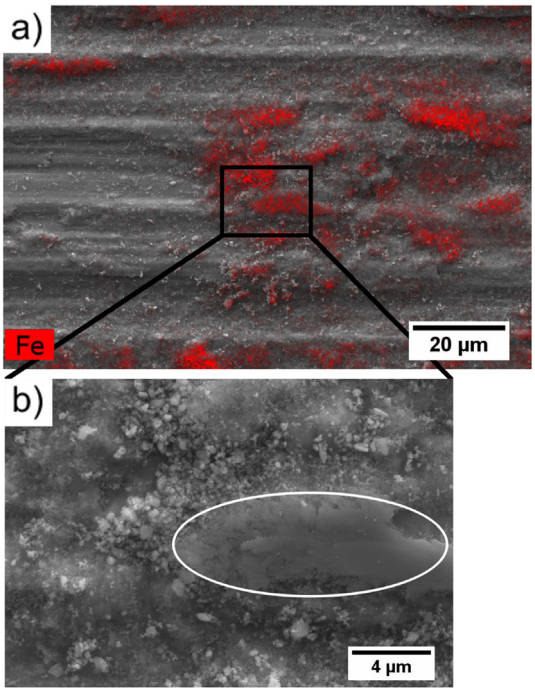

Fig. 6. SEM image of the wear groove after 10000 cycles on initial sample stopped during Stage III (a) with Fe (red) EDS map in transparency and focus on accumulation and binding of Fe wear debris (b). White ellipse indicates high Fe concentration

the groove and by identification, as will be discussed in part 4.1., this peak is attributed to the TiO_2-anatase peak at 516 cm^{-1}. In Raman, the peaks may shift slightly from their positions and their intensities may vary differently depending on several parameters like the grain size [31] or the residual stress [32]. Thus, it is possible to find only a single peak in specific conditions, the others being hidden in the baseline. In order to avoid any unnecessary misinterpretation only the noticeable peaks are identified to the corresponding phases.

The spectrum taken in zone 2 (in dark in Fig. 8a) differs from the rest of the surface. Zone 2 shows a Raman spectrum with an additional broader peak observed from 650 to 750 cm^{-1}corresponding to the Fe-rich transfer layer formed during the friction. By identification this broad peak corresponds to the superposition of the three high intensity peaks of the Fe_2O_3-maghemite phase. The map in Fig. 8b confirmed that the Fe_2O_3-maghemite was the only Fe-rich oxide detected all along the elongated central band in the groove.

After 10 000 cycles (Fig. 8f), the Raman spectrum corresponding to zone 3 is similar to that obtained for zone 1, e.i. only TiO_2-anatase is present in these areas. Comparatively, the spectrum taken from zone 4 reveals several sharp peaks identified as the simultaneous presence of Fe_2O_3-maghemite and Fe_2O_3-hematite. The map in Fig. 8d shows the presence of the Fe_2O_3-hematite in the wear track at locations corresponding to the dark areas visible by optical microscopy. Further analyses revealed that Fe_2O_3-maghemite covered the same domains as Fe_2O_3-hematite, suggesting that the phase transformation toward the stable Fe_2O_3-hematite was in progress. This will be discussed in part 4.1.

Local SEM/EDS analyses have revealed that the debris formed during the wear process had different sizes depending on their chemistry. This is illustrated by Figs. 9a and b which show high resolution SEM images of respectively Ti-rich and Fe-rich wear debris collected after a 10 000 cycles test on the initial surface sample. Titanium-rich debris were on average larger than the Fe-rich ones. Debris obtained after 2000 and 10 000 cycles for both types of surfaces showed similar characteristics (not shown here). Observations also revealed some very large titanium debris (several tens of micrometers) with abrasion marks on them. These large Ti debris clearly came from the surface spalling during stage I. Representative Raman spectra obtained from five measurements on each of the titanium and iron debris are shown in Fig. 9. The spectra obtained from the Ti-rich debris showed not only the presence of TiO_2-anatase but also of TiO_2-rutile. However, even if Fe_2O_3-maghemite was identified in the wear grooves (Fig. 8e and f), Raman spectra only indicated the presence Fe_2O_3-hematite in the Fe-rich debris; as seen in the spectrum in Fig. 9c.

4. Discussion

The investigation of the tribological properties of a commercially pure Ti, with and without SMAT modification, revealed drastic changes in the evolution of the coefficient of friction as a function of the number of alternate cycles. This evolution consisted of three different stages with specific friction characteristics, independently if the surface was coarse grained or nanostructured. The major difference between the initial coarse grain structure and the ultrafine SMATed one was in the period taken to initiate the transition from one stage to the other. These behaviors could be interpreted by the formation of different oxides appearing at different times during the tribology tests that affected the wear mechanisms.

Thus, this discussion is divided into two parts. Firstly, the evolution of the coefficient of friction will be analyzed in connection with the formation of oxides and their implication in the wear mechanisms. Secondly, the effect of the strain hardening and grain refinement provided by SMAT modification on this friction behavior will be discussed.

4.1. Friction mechanisms and oxides formation

Our main findings in terms of friction mechanisms and oxides formation occurring during the different stages of wear are summarized in Fig. 10 in the form of a diagram with the links between each oxides following their order of appearance. For each stage, the main oxides

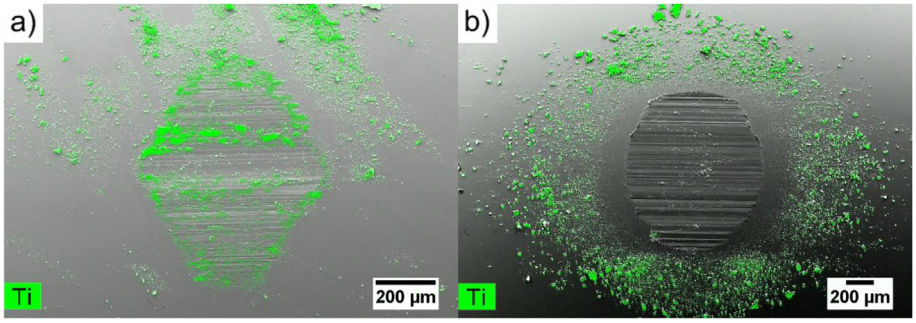

Fig. 7. SEM images of ball worn areas during friction tests for 2 000 cycles against SMATed sample stopped during Stage II (a) and against initially polished sample stopped during Stage III (b). Ti (green) EDS maps are in transparency above SEM images

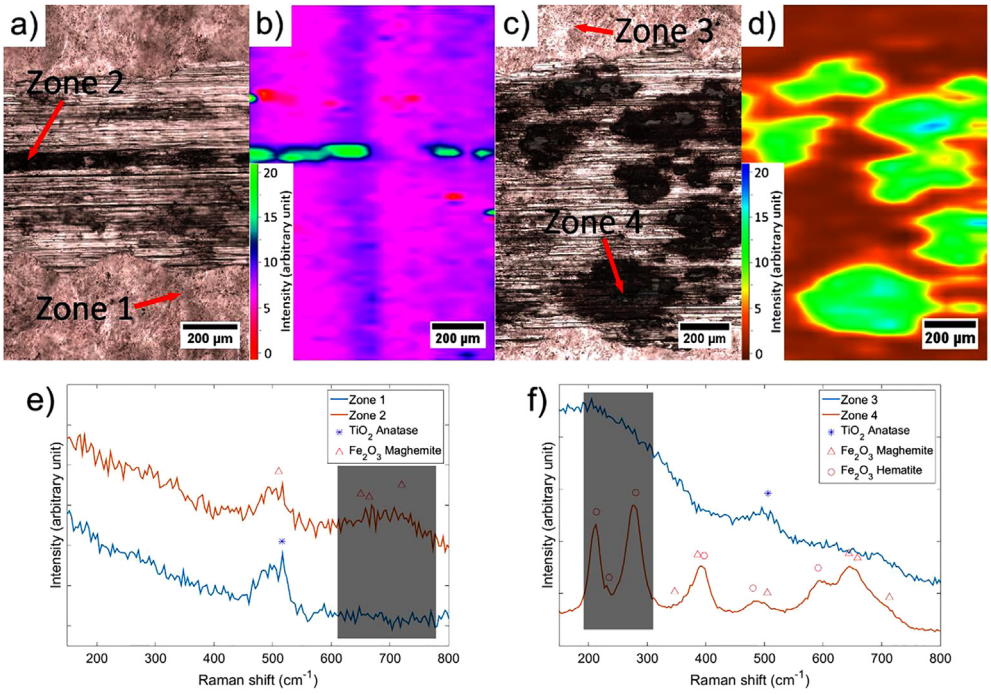

Fig. 8. Optical microscope image of the 2 000 cycles (a) and 10 000 cycles (c) grooves on SMATed surface with corresponding reconstructed images from Raman mappings (b) and (d). Raman spectra (e) and (f) corresponding respectively to zones 1 and 2 in (a) and to zones 3 and 4 in (c). Relevant oxides peaks are also indicated in (e) and (f)

that formed and were responsible for the characteristic friction behavior are represented. Their formation mechanisms and their effect on the wear behavior and damaging of the two bodies in contact are discussed in the following discussion.

At the beginning of the friction tests, the coefficient of friction increased quickly corresponding to the break-in period [33]. After the break-in, the coefficient of friction reached values of around 0.5 corresponding to stage I. Similar results were previously reported by Wen et al. [25] and by Alikhani Chamgordani et al. [22] respectively for nanostructured and coarse grained commercially pure Ti surfaces. The coefficient of friction remained in a steady-state for at least several hundreds of cycles independently of the surface condition. This behavior is mainly dominated by the wear of the titanium sample with nearly no damage to the steel counterface. As it was seen in Fig. 5a, the groove formed on titanium showed no trace of iron. During stage I a titanium transfer layer appears on the surface of the steel ball. This friction behavior corresponds to the contact between a high strength steel ball onto fresh surface of the commercially pure titanium. The debris generated are then oxidized into titanium oxides. Oxidation has also been reported in the pioneer work of Molinari et al. [34] who have analyzed the oxidative wear of the Ti6Al4V alloy and demonstrated that the amount of oxide that formed depends on the applied load and sliding speed. One of the complementary results obtained in the present work, under our experimental conditions, concerns the nature of the different oxides that formed under sliding and the fact that their nature changed progressively. Indeed, while TiO_2-anatase is the main titanium oxide generally encountered at room temperature [35], the presence of TiO_2-rutile was also detected here. It is well established that TiO_2-rutile is a titanium oxide formed at elevated temperature, over 500 °C [35]. Thus, the presence of TiO_2-rutile suggests a high local elevation of the temperature in the contact. The main source of heat is the deformation of the surfaces during friction which depends on the sliding conditions. The low thermal diffusivity of titanium also plays an important role for this temperature increase since it made it difficult to dissipate the heat through the material. Abukhshim discussed this phenomenon as a main problem in machining [36]. Straffelini et al. showed also that, under given sliding conditions on the Ti6Al4V alloy, the amount of heat generated depended on the nature of the counterface [37]. Shakhvorostov et al. have measured the temperature of less than 200 °C under lubricated condition on Al-SI/steel tribo-contacts for a sliding speed of 0.35 m/s [38]. Comparatively, microstructure modifications indicated values of more than 600 °C under dry sliding conditions at 7 m/s for Ti/steel contact [39]. In addition to the effect of temperature, it is quite possible that the pressure on plastic strain can have an effect on the ability to form rutile under local high pressure tribological conditions. For example, Edalati et al. have shown that unlike static annealing in which the anatase to rutile phase transformation occurred at 900 °C, the transformation was observed at low (200–300 °C) under SPD obtained by HPT [40]. As will be discussed in part 4.2, the results revealed a marked difference in the friction of the SMATed and initial samples. However, both allowed the temperature to increase and, in both cases, this provoked a modification of the coefficient of friction when the temperature reached a high enough threshold for the titanium oxide to change from TiO_2-anatase to TiO_2-rutile.

The TiO_2-anatase hardness was reported to be between 616 and 698 HV [41], not high enough to damage the steel ball counterface of 840 HV. On the other hand, the TiO_2-rutile hardness was reported between 894 and 974 HV [41]. Thus, TiO_2-rutile is then able to erode the steel ball surface, forming the first steel debris inducing changes in wear mechanism and coefficient of friction, this is the transition towards stage II. An Fe-rich transfer layer formed at the groove bottom, as can be seen in Fig. 5b. However, a large titanium transfer layer was still observed onto the steel surface (Fig. 7a). The titanium wear debris were larger than the Fe-rich ones and presented facets whereas Fe-rich particles seemed to be strongly bonded to each others. These Fe-rich debris also formed aggregates; promoting thereby the formation of the Fe-rich transfer layer in the groove. The oscillations of the coefficient of friction, varying between higher (0.8) and lower (0.5) values, essentially during stage II in Fig. 2 (or punctually stage III in Fig. 2a) can be understood by this modification of transfer layer and, thus, the nature of third body involved during sliding. The lower values, close to that of the stage I, are associated to the same mechanisms identified during stage I: abrasion of the titanium surface with a continuous sliding motion, as seen in Fig. 5a. Comparatively, the higher values are attributed to a change from sliding to stick-slip behavior provoked by the formation of the Fe-rich transfer layer onto the Ti surface; the wear is then characterized by a strong adhesion of the newly formed Fe-oxide layer with the steel ball (as Fig. 5b suggests). As the number of oscillations

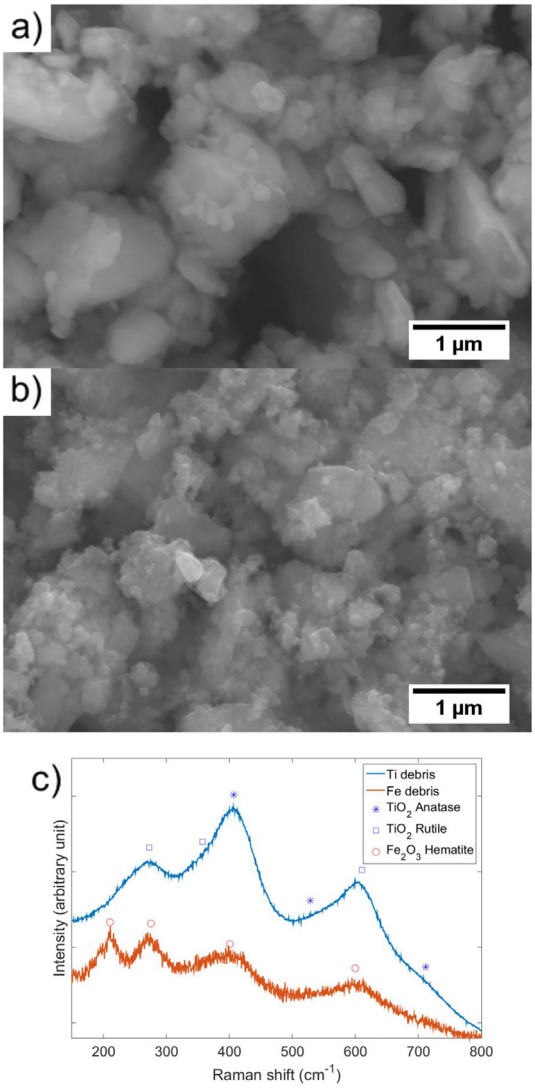

Fig. 9. High resolution observations of Ti debris (a) and Fe debris (b) obtained after 2 000 cycles on the initially polished sample and Raman spectra of Ti and Fe debris with relevant oxides peaks (c)

increases, more cycles were spent at the highest values (Fig. 2) and the newly formed Fe-rich transfer layer covered a larger area in the groove.

The Raman analyses (Fig. 8) suggest that the Fe-rich transfer layer is formed from Fe_2O_3-maghemite oxide during the stage II. Based on the literature, this oxide is mainly formed during the oxidation cycle of iron [42,43]. The successive oxidation reactions of iron form first the FeO-wüstite, then it is transformed into the Fe_3O_4-magnetite and finally the Fe_2O_3-maghemite appears as the iron oxidation increases [42].The high oxidation degree makes Fe_2O_3-maghemite metastable in its cubic form and it turns into an hexagonal structure of Fe_2O_3-hematite when the local contact temperature is high enough [44]. The Fe_2O_3-hematite is the most stable iron oxide with the highest oxidation degree. It is very interesting to note that the Fe_2O_3-maghemite appears to have an affinity with titanium and titanium oxides; indeed the natural presence of TiO_2-anatase was reported in Fe_2O_3-maghemite ores [41]. Also, another oxide named $Fe(Fe,Ti)_2O_4$-titanomaghemite having the same space group as Fe_2O_3-maghemite with Ti atoms substituting Fe atoms has also been reported, confirming this affinity [45]. This may explain why the Fe-rich transfer layer formed easily on the Ti surface and why the Fe oxide on the titanium surface was composed of the metastable Fe_2O_3-maghemite rather than being transformed into the stable Fe_2O_3-hematite. The presence of TiO_2-anatase would thus stabilize the Fe_2O_3-maghemite. This also explains why only the Fe_2O_3-hematite is visible in the debris: without TiO_2-anatase the Fe_2O_3-maghemite became unstable enough to transform into Fe_2O_3-hematite. The hardness values of the Fe_2O_3-maghemite and Fe_2O_3-hematite are 920 HV and 1000–1100 HV, respectively [41]. Both values are high enough to induce damage on the steel ball counterface. While the titanium oxides were continuously formed on the titanium fresh surfaces in the early stages of the wear process, when the steel transfer layer is large enough to prevent most direct contacts between the steel ball and the titanium surface the coefficient of friction becomes stabilized, reaching a new steady-state. This marks the end of stage II - characterized by significant fluctuations in Fig. 2 - and the beginning of the steady state stage III.

In stage III, the friction is dominated by the contact between the deposited iron oxides and the steel ball leading to a highly stable steady-state. The only additional damage that could occur at the titanium surface were found on the sides of the groove where fresh Ti surfaces were located. Because of the increased generation of iron oxides, the titanium transfer layer on the ball was not maintained and disappeared. As the steel ball was worn, the Fe-rich debris must have oxidized into FeO-wüstite, then Fe_3O_4-magnetite and quickly turned into Fe_2O_3-maghemite, forming large patches on the groove (Fig. 8d). Ultimately, the iron oxide changed into Fe_2O_3-hematite which was slowly chased away from the transfer layer under the form of wear debris that deposited at the periphery of the groove. This cycle

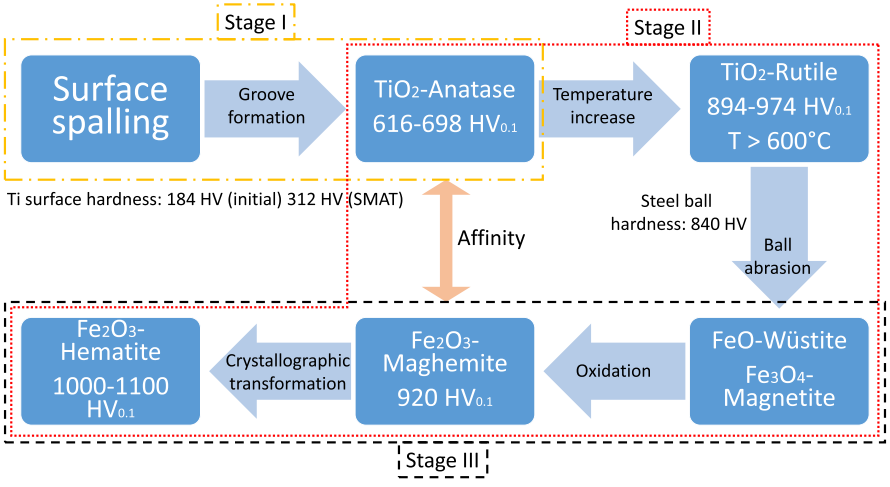

Fig. 10. Theory of oxides formation during the friction and identification of stages depending on the main mechanisms involved

continues steadily, as proved by the stable coefficient of friction. A thorough observation of Fig. 2 revealed a slow increase in the coefficient of friction. Wang et al. [46] saw a similarly slight increase in the coefficient of friction for the contact of an H-11 tool steel ball on an Al-7475 alloy and explained it, comforted by analytical calculations, by the increase in groove width. Interestingly, short temporary drops of the coefficient of friction could also be observed in stage III, as seen more particularly in Fig. 2a. The values at which the coefficient of friction dropped were the same as those measured during stage I. Thus, they can be interpreted as a characteristic of the friction of the steel ball onto a new titanium surface due to a fracture of the Fe-rich transfer layer leaving a fresh titanium surface at the bottom of the groove. The temperature in this region being high enough, the hard titanium TiO_2-rutile oxide reforms quickly and the process of wear of the steel ball and formation of a new steel transfer layer is repeated.

4.2. Effect of surface nanostructured by SMAT on the friction behavior

After a given similar tribology test, the nanostructured SMATed Ti surfaces have sustained more pronounced damages characterized, for example, by a wear loss twice as high compared to that of the initially polished coarse grained surfaces (Table 1). However, the wear of the steel ball was greatly reduced when it slid against the hard SMATed surfaces as compared to the initial surfaces (Table 2). These counter intuitive differences in mechanical behavior can be understood by considering the effect of the material state on the kinetics of formation of the abrasive oxides that, in turn, affect the time of occurrence and length of the different friction stages that were depicted in the previous section.

The delayed transition toward the wear of the steel ball (length of stages I + II) in the case of the SMATed surface is due to the delayed formation of the hard Ti oxide which is, itself, attributed to a lower amount of heat generation during the rubbing onto the SMATed surfaces. Indeed, this type of surface has been hardened (Table 1) by the severe plastic deformation encountered during SMAT and has, consequently, a higher yield strength than its initially polished homolog. Thus, under similar fixed wear loading conditions, the already hardened SMATed surface sustained a lower amount of plastic deformation than the initial polished surface and, possibly, less adiabatic heating was also generated at the passage of the sliding ball onto the SMATed surface. As a consequence, the hard TiO_2-rutile debris formed and started their abrasive action later in the sliding process for the SMATed surfaces. Thus, the steel ball was ultimately less damaged when it was sliding on the nanostructured and hard Ti SMATed surface than on the coarse grained Ti one. Also, in consequence, the Fe-rich transfer layer protecting the Ti sub-surface appeared later for the SMATed surfaces. Thus, overall, for the same number of cycles, more time has been spend wearing the Ti surface during the stage I and II for the SMATed surfaces; leading to deeper grooves for the hard and nanostructured Ti SMATed sample than for the coarse grained material.

The rather broad ranges of occurrences for the transitions T1 and T2 (Fig. 3) as well as the broad range of maximum depth (Fig. 4b) obtained for the tests carried out on the SMATed samples are also interesting features. These discrepancies are attributed to the high roughness of the SMATed surfaces (Rz = 20 µm in Table 1) which leads to high variations in local contact pressures and, consequently, a wider variability of (i) the local thermal gradients and (ii) the intensity of surface spalling from one experiment to another. However, even if each groove may lead to large variations in the values of T1 and T2 as well as in the average wear depth for a SMATed sample, the same wear mechanisms - driven by the oxide modifications - came into play during the different stages of wear for the initial coarse grains and nanostructured SMATed samples.

As was mentioned in the introduction of this manuscript, several previous investigations of SMATed surfaces have revealed apparently contradicting results for Mg and steel. The same type of apparently contradicting results are revealed here in the case of commercially pure TI (CP-Ti). Indeed, considering the comparative wear of a CP-Ti metal with and without SMAT, Alikhani Chamgordani et al. [22] have clearly reported a reduction of 60% in volume loss after the application of the SMAT process, an opposite trend to the one presented here that revealed a negative effect of SMAT. Having presently clearly established the effect of the nature of the third body oxide layers present at the CP-Ti/steel ball interface, it is now possible to explain fully coherently these apparently conflicting results. In their work, Alikhani Chamgordani et al. [22] have used a SMAT machine with a steel chamber in which the shots were set in motion via a mechanical device [22,47]. It was confirmed by XRD and EDS analyses that a fairly large amount of Fe and FeO contamination was deposited on the surface of the samples when they were SMAT treated with this machine [22]. This contamination originated from the abrasion of balls and contained interior walls [22]. Consequently, when the tribology tests are carried out, the material surface has already the characteristics that are encountered here during stage III: the Fe and Fe-rich oxides debris produced during SMAT have created a third body acting as a kind of protective layer on the Ti surface. Thus, wear was less effective on these Fe-SMAT-contaminated surfaces than on the clean ones (without SMAT). Comparatively, the machine used in the present investigation uses a piezoelectric power supply that is moving a Ti-6Al-4V sole that, itself, sets the shots in motion [26]. Transmission electron microscopy and glow discharge - optical emission spectroscopy have revealed a contamination reach in Ti with a little of Al and V at the surface of the steel samples treated with this ultrasonic SMAT device [48]. Thus, under the condition of the present study, the essential Ti-rich contamination did not change drastically the chemical nature of the surface and the effect of the Ti nanostructure created by the ultrasonic-SMAT was clearly revealed.

Thus, it is likely that several apparently contradicting results obtained in previous investigations of the wear of SMATed surfaces can be explained by taking into account the exact nature of the contamination - originated from the abrasion of balls and internal walls of the SMAT device - occurring during the SMAT treatment process.

5. Conclusions

The aim of this study was to improve our understanding of the friction behavior and wear mechanisms of commercially pure titanium sliding with an alternate motion against a steel counterface. Significant variations in the friction behavior were observed and attributed to modifications in wear mechanisms that were essentially driven by successive changes in the nature of the third body oxides created throughout the tribology tests. The effect of a nanostructure within the Ti surface, generated here by SMAT, was also tested. The main outcomes in the friction and wear behaviors can be summarized as follows:

- Significant wear of the steel counterface was observed at the end of the tests even if the hardness of the steel ball was much higher than the titanium surface (i.e. 840 HV against 188 HV for the coarse grained Ti sample or 282 HV for the nanostructured Ti surfaces, respectively). This was attributed to the formation of the high hardness TiO_2-rutile oxide during the friction tests.
- Modifications in the nature of the oxides formed at the surface of the Ti samples from Ti-rich (TiO_2-anatase then TiO_2-rutile) to Fe-rich (Fe_2O_3-maghemite then Fe_2O_3-hematite) oxides could explain the transitions in the coefficient of friction. When resulting from a contact with the titanium or titanium oxides, the metastable Fe_2O_3-maghemite seems to be stabilized in the Ti-wear tracks.
- Each transition in the oxide modification was found to affect the wear behavior and to lead to different successive friction stages after the short initial break-in period. The main features of each stage are listed below:

• Stage I - A rather stable coefficient of friction is established when the steel ball slides against the titanium surface. The wear of the

titanium surface generates the formation of TiO_2-anatase which is accompanied by a gradual and steady increase of the coefficient of friction. The TiO_2-anatase subsequently transforms into TiO_2-rutile; which also induces the transition towards stage II.

- Stage II - Significant fluctuations in the values of friction coefficient are here recorded. The formation of hard TiO_2-rutile debris explains the wear of the steel ball and the formation of Fe-rich oxides. The formation of Fe_2O_3-hematite generated a Fe-rich oxide transfer layer on the titanium surface; which initiated the stage III.
- Stage III - A stable coefficient of friction is established as the steel ball is sliding against the Fe-rich third body transfer layer that is acting as a kind of protective layer on the Ti surface.

- Under similar dry sliding tribology testing conditions, the nanostructured surfaces obtained by SMAT have led to high hardness values but, in a rather counter intuitive manner, to a detrimental wear behavior. As the formation of abrasive hard oxides was delayed when rubbing was done on the SMATed nanostructured surface, the wear of the steel ball counterface was less pronounced. As these hard oxides ultimately produced a third body protective layer on the Ti surfaces, its delayed formation onto the SMATed nanostructured Ti surface led to values of the wear losses twice those obtained for steel ball sliding against the softer Ti surface.

- A sound analysis of apparently contradicting results obtained in previous investigations of the wear of SMATed surfaces can be explained by taking into account the exact nature of a contamination that can form during this treatment because of the abrasion of the balls and internal walls of the SMAT device.

Funding

This work was supported by the French Government through the program “Investissements d'avenir” operated by the French National Research Agency (ANR) and referenced to as ANR-11-LABX-0008-01 (‘LabEx DAMAS’). This work was also supported by the Laboratory of Optimization of Advanced Processes and Fabrication (LOPFA, Montréal, Canada).

Acknowledgements

The authors would like to acknowledge Dr. Mathieu Marquer for his valuable help in running the tribology tests and Dr. Thomas Kauffmann for his assistance in using Raman spectroscopy, and also for the valuables insights and discussions they both provided. Raman measurements were performed at the spectroscopy platform of the LMOPS, Université de Lorraine & CentraleSupélec.

References

[1] Y. Estrin, A. Vinogradov, Extreme grain refinement by severe plastic deformation: a wealth of challenging science, Acta Mater. 61 (2013) 782–817, https://doi.org/10.1016/j.actamat.2012.10.038.
[2] T.C. Lowe, R.Z. Valiev, The use of severe plastic deformation techniques in grain refinement, Jom 56 (10) (2004) 64–68, https://doi.org/10.1007/s11837-004-0295-z.
[3] I.A. Ovid’ko, R.Z. Valiev, Y.T. Zhu, Review on superior strength and enhanced ductility of metallic nanomaterials, Prog. Mater. Sci. 94 (2018) 462–540, https://doi.org/10.1016/j.pmatsci.2018.02.002.
[4] R.Z. Valiev, T.G. Langdon, Principles of equal-channel angular pressing as a processing tool for grain refinement, Prog. Mater. Sci. 51 (2006) 881–981, https://doi.org/10.1016/j.pmatsci.2006.02.003.
[5] K. Edalati, Z. Horita, A review on high-pressure torsion (HPT) from 1935 to 1988, Mater. Sci. Eng. A 652 (2016) 325–352, https://doi.org/10.1016/j.msea.2015.11.074.
[6] Y. Saito, N. Tsuji, H. Utsunomiya, T. Sakai, R. Hong, Ultra-fine grained bulk aluminum produced by accumulative roll-bonding process, Scripta Mater. 40 (1999) 795–800, https://doi.org/10.1016/S1359-6462(98)00302-9.
[7] H.Y. Miao, D. Demers, S. Larose, C. Perron, M. Lévesque, Experimental study of shot peening and stress peen forming, J. Mater. Process. Technol. 210 (2010) 2089–2102, https://doi.org/10.1016/j.jmatprotec.2010.07.016.
[8] C.S. Montross, T. Wei, L. Ye, G. Clark, Y.W. Mai, Laser shock processing and its effects on microstructure and properties of metal alloys: a review, Int. J. Fatigue 24 (2002) 1021–1036, https://doi.org/10.1016/S0142-1123(02)00022-1.
[9] R.L. Murthy, B. Kotiveerachari, Burnishing of metallic surfaces - a review, Precis. Eng. 3 (1981) 172–179, https://doi.org/10.1016/0141-6359(81)90010-6.
[10] K. Lu, J. Lu, Nanostructured surface layer on metallic materials induced by surface mechanical attrition treatment, Mater. Sci. Eng. A 375 (2004) 38–45, https://doi.org/10.1016/j.msea.2003.10.261.
[11] N.R. Tao, M.L. Sui, J. Lu, K. Lua, Surface nanocrystallization of iron induced by ultrasonic shot peening, Nanostruct. Mater. 11 (1999) 433–440, https://doi.org/10.1016/S0965-9773(99)00324-4.
[12] X. Liu, K. Wu, G. Wu, Y. Gao, L. Zhu, Y. Lu, et al., High strength and high ductility copper obtained by topologically controlled planar heterogeneous structures, Scripta Mater. 124 (2016) 103–107, https://doi.org/10.1016/j.scriptamat.2016.07.003.
[13] S. Xia, Y. Liu, D. Fu, B. Jin, J. Lu, Effect of surface mechanical attrition treatment on tribological behavior of the AZ31 alloy, J. Mater. Sci. Technol. 32 (2016) 1245–1252, https://doi.org/10.1016/j.jmst.2016.05.018.
[14] Y. Liu, B. Jin, D. Li, X. Zeng, J. Lu, Wear behavior of nanocrystalline structured magnesium alloy induced by surface mechanical attrition treatment, Surf. Coating. Technol. 261 (2015) 219–226, https://doi.org/10.1016/j.surfcoat.2014.11.026.
[15] V. Pandey, K. Chattopadhyay, N.C.S. Srinivas, V. Singh, Role of ultrasonic shot peening on low cycle fatigue behavior of 7075 aluminium alloy, Int. J. Fatigue 103 (2017) 426–435, https://doi.org/10.1016/j.ijfatigue.2017.06.033.
[16] A.Y. Chen, H.H. Ruan, J. Wang, H.L. Chan, Q. Wang, Q. Li, et al., The influence of strain rate on the microstructure transition of 304 stainless steel, Acta Mater. 59 (2011) 3697–3709, https://doi.org/10.1016/j.actamat.2011.03.005.
[17] Y. Sun, Sliding wear behaviour of surface mechanical attrition treated AISI 304 stainless steel, Tribol. Int. 57 (2013) 67–75, https://doi.org/10.1016/j.triboint.2012.07.015.
[18] Y. Samih, B. Beausir, B. Bolle, T. Grosdidier, In-depth quantitative analysis of the microstructures produced by Surface Mechanical Attrition Treatment (SMAT), Mater. Char. 83 (2013) 129–138, https://doi.org/10.1016/j.matchar.2013.06.006.
[19] M. Novelli, J.J. Fundenberger, P. Bocher, T. Grosdidier, On the effectiveness of surface severe plastic deformation by shot peening at cryogenic temperature, Appl. Surf. Sci. 389 (2016) 1169–1174, https://doi.org/10.1016/j.apsusc.2016.08.009.
[20] M. Novelli, P. Bocher, T. Grosdidier, Effect of cryogenic temperatures and processing parameters on gradient-structure of a stainless steel treated by ultrasonic surface mechanical attrition treatment, Mater. Char. 139 (2018) 197–207, https://doi.org/10.1016/j.matchar.2018.02.028.
[21] K.Y. Zhu, A. Vassel, F. Brisset, K. Lu, J. Lu, Nanostructure formation mechanism of α-titanium using SMAT, Acta Mater. 52 (2004) 4101–4110, https://doi.org/10.1016/j.actamat.2004.05.023.
[22] S. Alikhani Chamgordani, R. Miresmaeili, M. Aliofkhazraei, Improvement in tribological behavior of commercial pure titanium (CP-Ti) by surface mechanical attrition treatment (SMAT), Tribol. Int. 119 (2018) 744–752, https://doi.org/10.1016/j.triboint.2017.11.044.
[23] P. La, Q. Xue, R.Z. Valiev, Dry-sliding tribological properties of ultrafine-grained Ti prepared by severe plastic, Deformation 53 (2005) 5167–5173, https://doi.org/10.1016/j.actamat.2005.07.031.
[24] K. Edalati, M. Ashida, Z. Horita, T. Matsui, H. Kato, Wear resistance and tribological features of pure aluminum and Al-Al2O3 composites consolidated by high-pressure torsion, Wear 310 (2014) 83–89, https://doi.org/10.1016/j.wear.2013.12.022.
[25] M. Wen, C. Wen, P.D. Hodgson, Y.C. Li, Tribological behaviour of pure Ti with a nanocrystalline surface layer under different loads, Tribol. Lett. 45 (2012) 59–66, https://doi.org/10.1007/s11249-011-9862-y.
[26] SONATS Europe Technologies group, Sonats Contact, (2019) http://www.sonats-et.fr/.
[27] G.A. Tompsett, G.A. Bowmaker, R.P. Cooney, J.B. Metson, K.A. Rodgers, J.M. Seakins, The Raman spectrum of brookite, TiO2 (Pbca, Z = 8), J. Raman Spectrosc. 26 (1995) 57–62, https://doi.org/10.1002/jrs.1250260110.
[28] L.J. Oblonsky, T.M. Devine, A surface enhanced Raman spectroscopic study of the passive films formed in borate buffer on iron, nickel, chromium and stainless steel, Corros. Sci. 37 (1995) 17–41, https://doi.org/10.1016/0010-938X(94)00102-C.
[29] M. Godet, The third-body approach: a mechanical view of wear, Wear 100 (1984) 437–452, https://doi.org/10.1016/0043-1648(84)90025-5.
[30] J. Heinrichs, M. Olsson, I.Z. Jenei, S. Jacobson, Transfer of titanium in sliding contacts-New discoveries and insights revealed by in situ studies in the SEM, Wear 315 (2014) 87–94, https://doi.org/10.1016/j.wear.2014.04.006.
[31] G.R. Hearne, J. Zhao, A.M. Dawe, V. Pischedda, M. Maaza, M.K. Nieuwoudt, et al., Effect of Grain Size on Structural Transitions in Anatase TiO 2 : A Raman Spectroscopy Study at High Pressure vol. 134102, (2004), pp. 1–10, https://doi.org/10.1103/PhysRevB.70.134102.
[32] I.A. Alhomoudi, G. Newaz, Residual stresses and Raman shift relation in anatase TiO2thin film, Thin Solid Films 517 (2009) 4372–4378, https://doi.org/10.1016/j.tsf.2009.02.141.
[33] S.C. Tung, H. Gao, Tribological characteristics and surface interaction between piston ring coatings and a blend of energy-conserving oils and ethanol fuels, Wear 255 (2003) 1276–1285, https://doi.org/10.1016/S0043-1648(03)00240-0.
[34] A. Molinari, G. Straffelini, B. Tesi, T. Bacci, Dry sliding wear mechanisms of the Ti6Al4V alloy, 208 (1997) 105–112, https://doi.org/10.1016/S0043-1648(96)07454-6.
[35] D.A.H. Hanaor, C.C. Sorrell, Review of the anatase to rutile phase transformation, J. Mater. Sci. 46 (2011) 855–874, https://doi.org/10.1007/s10853-010-5113-0.
[36] N.A. Abukhshim, P.T. Mativenga, M.A. Sheikh, Heat generation and temperature

prediction in metal cutting : a review and implications for high speed machining, Int. J. Mach. Tool Manuf. 46 (2006) 782–800, https://doi.org/10.1016/j.ijmachtools.2005.07.024.
[37] G. Straffelini, A. Molinari, Dry sliding wear of Ti-6Al-4V alloy as influenced by the counterface and sliding conditions, Wear 236 (1999) 328–338, https://doi.org/10.1016/S0043-1648(99)00292-6.
[38] D. Shakhvorostov, et al., Correlated wear measurements using gold implantation, backscattering, nuclear activation analysis and profilometry, Tribol. Int. 44 (2011) 737–750.
[39] L. Maire, et al., Influence of duplex USSP/Nitriding surface treatments on the dry sliding behavior of Ti6Al4V/AISI 316L tribopairs, Procedia Eng. 114 (2015) 621–626.
[40] K. Edalati, et al., Low-temperature anatase-to-rutile phase transformation and unusual grain coarsering in titanium oxide nanopowders by high-pressure torsion straining, Scripta Mater. 162 (2019) 341–344.
[41] J.W. Anthony, R.A. Bideaux, K.W. Bladh, M.C. Nichols, Handbook of Mineralogy, Mineralogical Society of America, Chantilly, 2005.
[42] L.C.F. Blackman, A review of the structure and some magnetic properties of ferrites, J Electron. Control 1 (1955) 64–77, https://doi.org/10.1080/00207215508547358.
[43] U. Schwertmann, R.M. Cornell, Iron Oxides in the Laboratory. Preparation and Characterization, Second, Co. WILEY-VCH Verlag GmbH, D-69469 Weinheim, 2000, https://doi.org/10.1002/ange.19921041155 Federal Republic of Germany).
[44] O. Ozdemir, S.K. Banerjee, High temperature stability of Maghemite (γ-Fe2O3), Geophys. Res. Lett. 11 (1984) 161–164, https://doi.org/10.1029/GL011i003p00161.
[45] Mindat.org. Mineral database, (2019) http://www.mindat.org.
[46] L. Wang, Y. He, J. Zhou, J. Duszczyk, Effect of temperature on the frictional behaviour of an aluminium alloy sliding against steel during ball-on-disc tests, Tribol. Int. 43 (2010) 299–306, https://doi.org/10.1016/j.triboint.2009.06.009.
[47] A. Heydari, R. Miresmaeili, S. Bagherifard, M. Guagliano, M. Aliofkhazraei, Incorporating the principles of shot peening for a better understanding of surface mechanical attrition treatment (SMAT) by simulations and experiments, Mater. Des. 116 (2017) 365–373, https://doi.org/10.1016/j.matdes.2016.12.045.
[48] Y. Samih, M. Novelli, T. Thiriet, B. Bolle, N. Allain, J.-J. Fundenberger, et al., Plastic deformation to enhance plasma-assisted nitriding : on surface contamination induced by surface mechanical attrition treatment, proceedings of the 6th international conference on nanomaterials by severe plastic deformation, IOP Conf. Ser. Mater. Sci. Eng. 63 (2014), https://doi.org/10.1088/1757-899X/63/1/012020.